

Cite this: *Energy Environ. Sci.*,
2019, 12, 2286

A new family of cation-disordered Zn(Cu)–Si–P compounds as high-performance anodes for next-generation Li-ion batteries†

Wenwu Li,^{ab} Xinwei Li,^{*c} Jun Liao,^a Bote Zhao,^{bd} Lei Zhang,^b Le Huang,^{id a}
Guoping Liu,^a Zaiping Guo,^{id d} and Meilin Liu,^{id *b}

The development of low-cost, high-performance anode materials for Li-ion batteries (LIBs) is imperative to meet the ever-increasing demands for advanced power sources. Here we report our findings on the design, synthesis, and characterization of a new cation-disordered ZnSiP₂ anode. When tested in LIBs, the disordered phase of ZnSiP₂ demonstrates faster reaction kinetics and higher energy efficiency than the cation-ordered phase of ZnSiP₂. The superior performance is attributed to the greater electronic and ionic conductivity and better tolerance against volume variation during cycling, as confirmed by theoretical calculations and experimental measurements. Moreover, the cation-disordered ZnSiP₂/C composite exhibits excellent cycle stability and superior rate capability. The performance surpasses all reported multi-phase anodes studied. Further, a number of the cation-disordered phases in the Zn(Cu)–Si–P family with a wide range of cation ratios show similar performance, achieving large specific capacities and high first-cycle coulombic efficiency while maintaining desirable working potentials for enhanced safety.

Received 23rd March 2019,
Accepted 10th May 2019

DOI: 10.1039/c9ee00953a

rsc.li/ees

Broader context

Developing low-cost, high-performance anodes for Li-ion batteries to replace the widely used graphite electrode is highly desirable to meet the ever-increasing demands for large capacity, high-rate capability, and long cycling life. Recently, anodes based on multi-phase composites have achieved improved energy density, cycling life, and rate performance compared to binary- or unary phase materials (*Energy Environ. Sci.*, 2017, 10, 1456–1464). Further, the constituent phases of the composites show a reversible synergistic effect during charge/discharge cycles. However, the synthesis of these complex compounds still faces the challenge of limited thermodynamic stability of the materials. Therefore, rational design of multi-phase materials with excellent electrochemical performance as well as cost-effective synthesis procedures is of great value to the development of new-generation Li-ion batteries.

Introduction

Li-Ion batteries (LIBs) are becoming a highly promising power source for many emerging technologies, including electric vehicles and smart grids.^{1–6} To meet the ever-increasing demands, it is imperative to develop low-cost anode materials with high

performance: high initial coulombic efficiency, large specific capacity, suitable working potential for safe operation, high-rate capability, and long-cycling life. Si-Based anodes have attracted much attention since it has potential to replace commercial grade graphite, benefiting from ultra-high gravimetric capacity (with a theoretical capacity of 4200 mA h g⁻¹, 11 times larger than that of a state-of-the-art graphite anode), low working potential, natural abundance in the crust of the earth, and mature processing infrastructure.^{7–13} However, the applicability of Si is limited by its low electronic and ionic conductivity and poor mechanical integrity due to large volume change during the lithiation/delithiation process. As a result, micro-sized Si anodes suffer from severe degradation in performance during cycling. To develop a robust electrode architecture with reliable electrochemical Li-storage performance, nanostructure engineering strategies have been applied to synthesize various advanced

^a School of Materials and Energy, Guangdong University of Technology, Guangzhou 51006, China

^b School of Materials Science and Engineering, Georgia Institute of Technology, Atlanta, Georgia 30332, USA. E-mail: meilin.liu@mse.gatech.edu

^c Department of Mechanical and Energy Engineering, Southern University of Science and Technology, Shenzhen, 518071, China. E-mail: lixw@sustech.edu.cn

^d Institute for Superconducting and Electronic Materials, School of Mechanical, Materials and Mechatronics Engineering, University of Wollongong, North Wollongong, NSW 2500, Australia

† Electronic supplementary information (ESI) available. See DOI: 10.1039/c9ee00953a

electrode architectures.^{14,15} Unfortunately, the sophisticated synthesis processes and low yield significantly increase the cost of Si-based batteries (cost per watt-hour, \$ per W h), thus limiting the practical applications of Si-based electrodes. Red P has also attracted considerable attention as an emerging anode material for rechargeable Li-, Na-, or K-ion batteries (with a theoretical capacity of 2596 mA h g⁻¹ corresponding to Li/Na/K₃P). However, the low electronic and ionic conductivity hinder its real application.^{16–19} To address this problem, various phosphor-carbon composites were proposed, e.g. red P/carbon nanotubes and amorphous P/carbon composites, where the carbon matrix serves as the current collector and mechanical-reinforcement backbone.^{20–24} However, synthesis of P/C composites often involves wet chemical methods, which require toxic P solvents and produce flammable white P.

An emerging strategy for creating synergistic effects between phases within a multi-phase composite has attracted some attention recently.^{25–31} For example, it has been reported that Fe/Co/Ni-SnO₂-graphite²⁵ and Sn₄P₃-SnSb-Sn²⁶ composites displayed better cycling stability and higher initial coulombic efficiency than those with only one or two phases. Compared to the multi-phase composites, a single-phase ternary compound (e.g., Bi₂MoO₆) could achieve much better electrochemical performance in a Li-ion battery due to atomic-level interface engineering and the electric-field effect.^{32,33} Similar synergistic effects were also reported for other ternary oxides and sulfides because of electrochemically derived multi-phase products.^{34–36} However, these ternary compounds usually show compromised electrochemical performance since each electrochemically derived product may have a distinctly different multi-step redox reaction mechanism. Additionally, the working potentials of ternary oxide and sulfide anodes are mainly above 1.0 V, resulting in low energy density. Also, it is challenging to synthesize these ternary compounds due to their limited thermodynamic stability. Therefore, rational design of ternary compounds with the right chemistry and proper working potentials requires a fundamental understanding of the structure-property relationship, which is urgent and crucial to the development of new battery technologies.

In this article, we report our findings on the design and synthesis of a cation-disordered ZnSiP₂ compound as a new-generation anode for LIBs. P and Zn were introduced into the structure of Si by virtue of their similar atomic sizes, bonding characteristics and electronegativity. The as-synthesized compound has a cation-disordered zinc blende or diamond-like structure, in which the introduced P and Si partially replace S sites and Zn sites, respectively, as confirmed by XRD refinement. The cation-disordered ZnSiP₂ anode delivered superior Li-storage properties compared to the cation-ordered ZnSiP₂ in terms of reaction kinetics, energy efficiency and cycling stability. The superiority was attributed to higher electronic and ionic conductivity as well as better resistance to volume change during cycling, as confirmed by first-principles calculations and electrochemical impedance spectroscopy. Furthermore, the cation-disordered ZnSiP₂ anode demonstrated an intriguing Li-storage mechanism with a peculiar reversibility back to its initial atomistic structure, as confirmed by *ex situ* XRD, TEM, Raman,

XPS, and electrochemical analysis. By further mixing with carbon, the resulting composite displayed impressive cycling performance with a specific capacity of 1789 mA h g⁻¹ after 500 cycles at 200 mA g⁻¹, and a superior rate capability with a capacity of 585 mA h g⁻¹ at a current density of 30 A g⁻¹. These excellent Li-storage performances are attributed to the excellent structural reversibility, fast Li-ion and electron transportation and the unique Li-storage mechanism. Furthermore, many compositions in the Zn(Cu)-Si-P family with various cation ratios displayed similar properties to those of the cation-disordered ZnSiP₂, including high initial coulombic efficiency, large capacity, and proper working potential between P/C and Si anodes.

The cation-ordered tetragonal phase ZnSiP₂, a typical ternary II-IV-V₂ semiconductor, is widely used in optoelectronics, spintronics, and quantum electronics.^{37–39} Nevertheless, its synthesis still adopts the complex and energy-consuming chemical vapor transport (CVT) and electrochemical synthesis method at about 1000 °C. In our study, we have successfully synthesized a new cation-disordered ZnSiP₂ phase with sphalerite structure in high yield by a facile mechanical ball milling process from the corresponding elemental powders as the raw materials. To investigate the phase evolution during the ball milling process, X-ray diffraction was performed to analyze the samples prepared with different milling times. As shown in Fig. 1a, after milling for 3 h, the main characteristic diffraction peaks of the sample can be assigned to ZnP₂, regardless of some residual Si raw material. After milling for 5 h, the peaks of the intermediate ZnP₂ and remaining Si raw material completely disappeared. All the observed peaks could be assigned to a Si-like structure with all the fingerprint peaks slightly shifted to higher 2 theta positions, compared to those of Si. With further increasing the milling time to 10 h, there were no significant changes in the XRD pattern. To explore its crystal structure, the related XRD Rietveld refinement is carried out. As shown in Fig. 1b, all diffraction peaks can be well-indexed by a new cubic phase in the *F* $\bar{4}3m$ space group.^{40,41} As shown in Fig. 1c, the refined cell parameters are identical to the ZnS structure counterparts, where Zn and Si atoms randomly occupy the Zn sites (of ZnS) and the P atoms occupy the S sites (of ZnS). The Zn and Si atoms are surrounded in a cubic manner by P atoms and *vice versa*. Details of the refinement including fractional atomic coordinates and cell parameters are shown in the inset of Fig. 1a and Tables S1 and S2 (ESI[†]). To probe more accurate local information on the crystal structure, we performed transmission electron microscopy (TEM). As shown in the TEM image (Fig. S1, ESI[†]) and its corresponding selected area electron diffraction (SAED, the inset of Fig. S1, ESI[†]), the clear ring-like pattern can also be well-assigned to the cubic ZnS crystal structure other than the typical tetragonal cells of the ternary II-IV-V₂ semiconductors, because of the lack of diffraction rings corresponding to the extra superstructures. More specifically, this kind of ZnS-like ZnSiP₂ phase can also be identified by easy observation of its exposed (110) and (1–10) crystal planes, as indicated by the spacing of lattice fringes in Fig. S2 (ESI[†]). The formation of the cation-disordered ZnSiP₂ probably resulted from the high pressure,

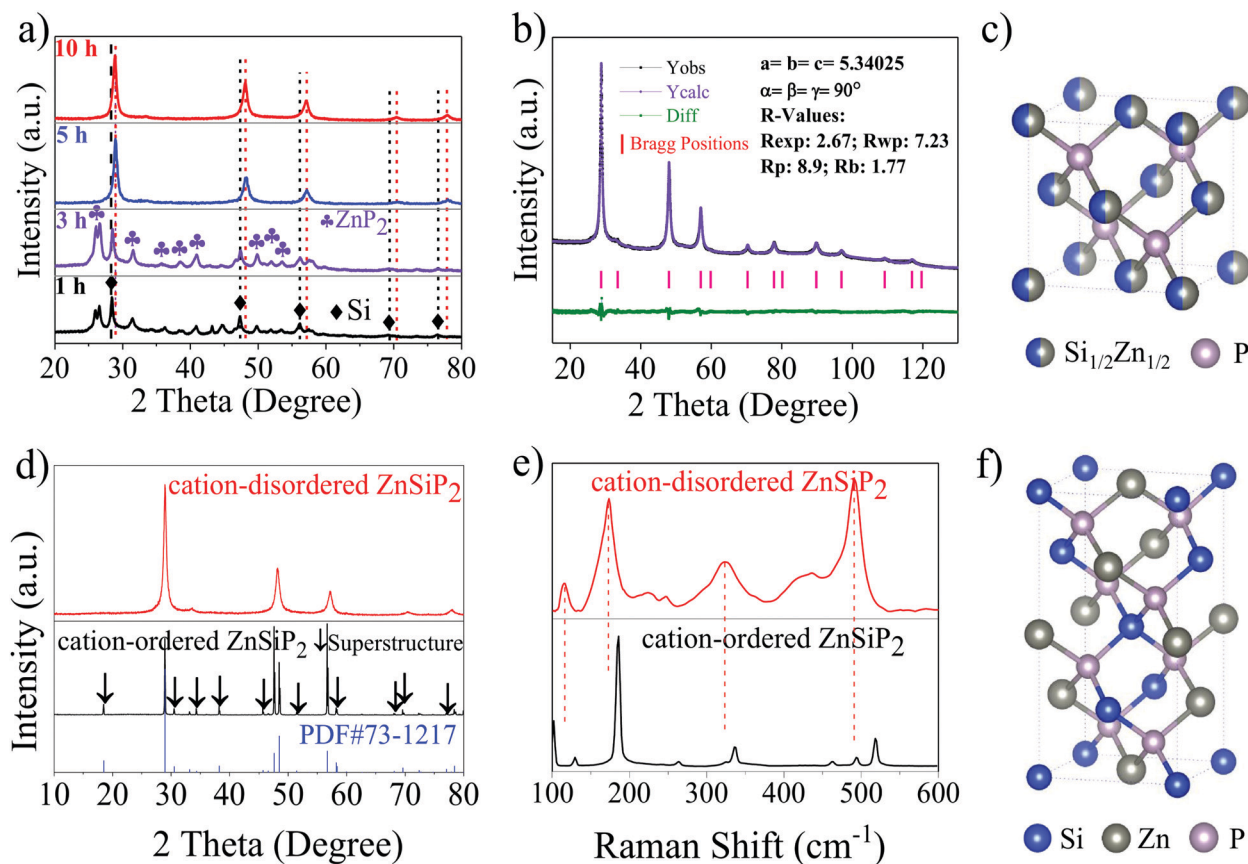


Fig. 1 (a) Evolution of the XRD patterns for a mixture of Zn–Si–P with a molar ratio of 1 : 1 : 2 as a function of ball milling time; (b) the XRD pattern for the Rietveld structure analysis of the stoichiometric cation-disordered ZnSiP_2 ; (c) a schematic crystal structure for the cation-disordered ZnSiP_2 ; (d) the XRD patterns of the cation-ordered ZnSiP_2 and cation-disordered ZnSiP_2 ; (e) the Raman spectra of the cation-ordered ZnSiP_2 and the cation-disordered ZnSiP_2 ; (f) a schematic crystal structure of the cation-ordered ZnSiP_2 .

high temperature and natural cooling rate generated by the high energy mechanical ball milling process.^{42,43} It is worth noting that the cation-disordered crystal structure has higher symmetry than the corresponding cation-ordered one, which is probably favorable to the long cycle life due to better stress accommodation.^{44,45} To compare the electrochemical performance difference of these two phases, we further synthesized the cation-ordered tetragonal phase of ZnSiP_2 . As shown in Fig. 1d, the peaks of the cation-ordered ZnSiP_2 phase substantially differ from those of the cation-disordered ZnSiP_2 due to the appearance of the extra superstructure. Raman spectroscopy (Fig. 1e) further demonstrated that the cation-ordered ZnSiP_2 phase indeed presents different modes, compared with the cation-disordered ZnSiP_2 counterparts, due to the delicate local environmental difference between these two phases (Fig. 1c and f).

Enlightened by the beneficial compositional and structural characterization, we anticipated that the cation-disordered ZnSiP_2 anode with several Li-reactive components would deliver attractive Li-storage properties with unique electrochemical behavioural features. Fig. 2a shows the initial three cyclic voltammetry (CV) curves of the cation-disordered ZnSiP_2 anode. During the initial cathodic scan, there is only one reduction band at the beginning of 0.50 V, which is attributed to the Li-ion uptake into the crystal

structural lattices of the cation-disordered ZnSiP_2 . In the subsequent anodic process, there is also only one relatively broader shoulder centered at 0.75 V, corresponding to the release of Li-ions from the electrode. It is noted that compared with the initial discharge profile (Fig. S3, ESI[†]), larger polarization was observed in the initial anodic CV scan, due largely to the relatively faster potential scan rate used for the CV measurements (Fig. S4, ESI[†]). In the subsequent two cycles, there is almost no change but the reduced polarization benefiting from the activation during the initial lithiation/de-lithiation process. During the initial electrochemical Li-storage process, defects are probably formed in the initial crystal structure, which would assist in the Li-ion transportation during the subsequent cycles.^{46,47} In other words, during the initial cycle, the crystal lattice must be relaxed or loosened, therefore it requires less activation energy to transport Li-ions during the subsequent cycles. By careful examination of the electrochemical Li-storage behaviours of the cation-disordered ZnSiP_2 anodes, there is no hint about the electrochemical Li-storage behavioural features of its single-component P, Si or Zn anodes as compared in Fig. S3 and S5 (ESI[†]) (initial discharge profiles at low current densities of 20 mA g^{-1} , etc.), which implies an intriguing Li-storage mechanism. As shown in Fig. S6 (ESI[†]), the initial discharge of the cation-disordered

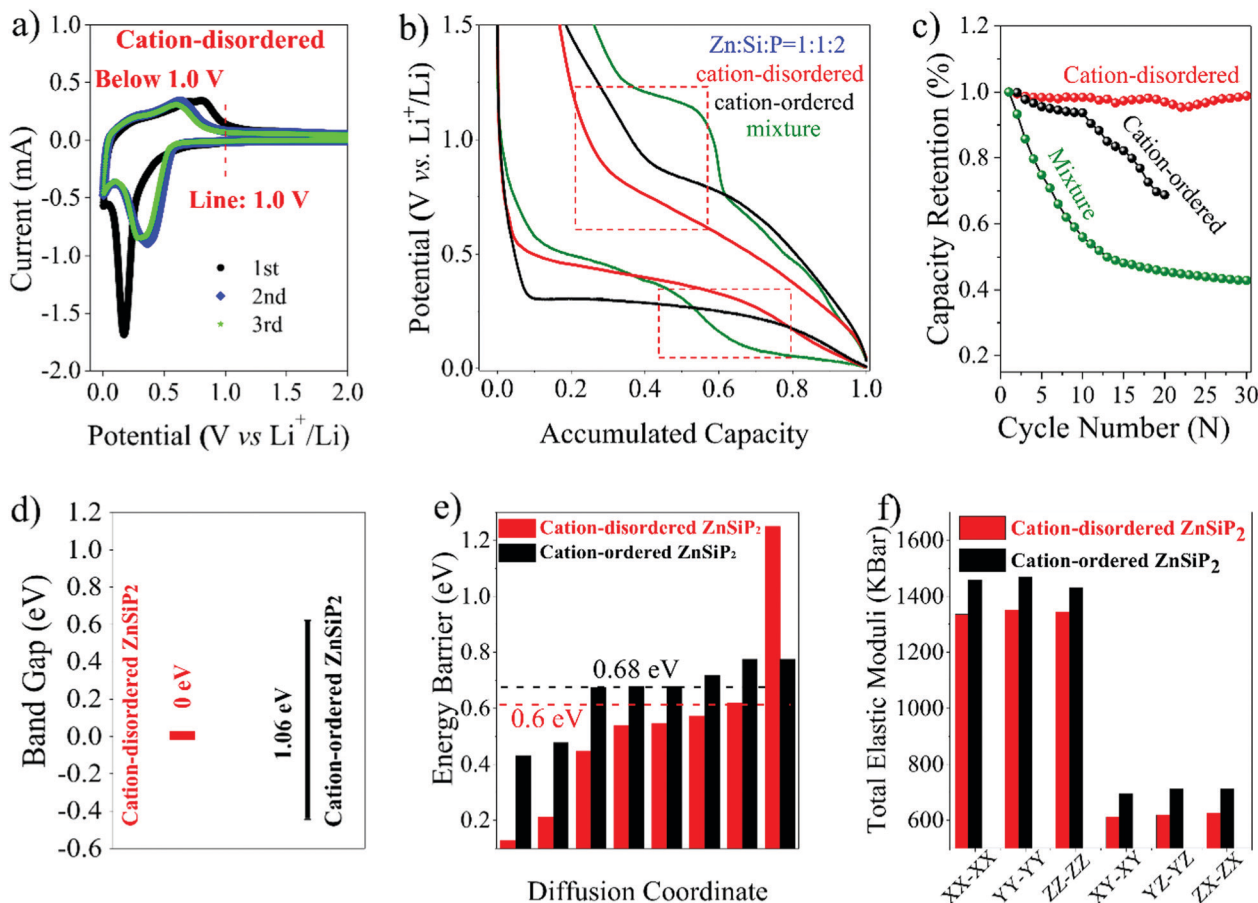


Fig. 2 (a) The initial three cyclic voltammetry (CV) curves of the cation-disordered ZnSiP₂ phase. (b) The first-cycle discharge/charge profile comparison; (c) the cycle performance comparison of the cation-disordered ZnSiP₂ phase, the intermediate product corresponded to ball milling of 3.0 h and the cation-ordered ZnSiP₂ phase also milled under the same experimental condition as the cation-disordered ZnSiP₂. (d) The band gap comparison; (e) the Li-ion activation energy comparison; (f) the elastic constant comparison of the cation-disordered ZnSiP₂ with the cation-ordered ZnSiP₂.

ZnSiP₂ electrode delivers a large capacity of *ca.* 2000 mA h g⁻¹ with only one low and safe working potential plateau of 0.40 V, thus avoiding dendrite growth like the commercially utilized graphite anode caused by the stripping of Li metal as the potential approached zero. During the subsequent charging process, the electrode can still achieve a specific capacity of 1860 mA h g⁻¹, which is five times larger than that of the commercial graphite anode. The first-cycle coulombic efficiency is up to 93%. From the second cycle onward (Fig. S6, ESI[†]), we can see that the reversible discharge/charge capacities can be maintained with little change in the discharge/charge profile shapes except for the relatively reduced polarization, compared with that of the initial cycle. All the electrochemical Li-storage behaviours exhibited by the galvanostatic discharge/charge profile of the cation-disordered ZnSiP₂ accord well with those presented by the corresponding CV curves (Fig. 2a) during the initial three cycles. To clearly show the unique advantages of the cation-disordered ZnSiP₂ anode, the initial discharge/charge features of the cation-disordered ZnSiP₂ are compared (Fig. 2b) with those of the cation-ordered ZnSiP₂ (prepared by CVT and then milled under the same conditions used for the cation-disordered ZnSiP₂) and an intermediate mixture corresponding to a ball milling time of 3.0 h.

The cation-disordered ZnSiP₂ anode shows the smallest polarization loss among the three anodes. During the charging process, the cation-disordered ZnSiP₂ did not show obvious multi-step reaction plateaus, and also the disappearance of the potential jump from 0.8 to 1.2 V for the cation-disordered ZnSiP₂ possibly benefits from its inherent faster reaction kinetics and peculiar Li-storage mechanism to be revealed.¹ As shown in Fig. 2c, the cycling stability of the cation-disordered ZnSiP₂ is also better than that of the intermediate mixture and the cation-ordered electrodes, profiting from its inherent structural advantages.

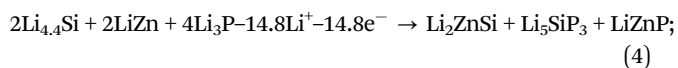
To track the fundamental reasons behind the electrochemical Li-storage superiority of the cation-disordered ZnSiP₂ to the cation-ordered ZnSiP₂ counterparts, we utilized first-principles calculations to provide more insights into the local environment to reveal the Li-ion and electron transport properties and resistance to structural variation.^{48–52} According to the cation-disordered structural features, we built a random-cation structure shown in Fig. S7a (ESI[†]).⁵³ For the electronic structure, to our surprise, as shown in Fig. 2d, the cation-disordered ZnSiP₂ has metallic conductivity featuring no band gap (Fig. S7b, ESI[†]). However, the cation-ordered ZnSiP₂ only shows a semi-conducting

feature with a band gap above 1.0 eV based on the simulated electronic structure shown in Fig. S7c and d (ESI[†]), which is consistent with the value reported before.³⁷ Therefore, we believe that the metallic conductivity of the as-synthesized ZnSiP₂ probably benefits from the cation disorder as revealed by various microscopic characterizations. To confirm the enhanced electron transport for the cation-disordered ZnSiP₂ predicted by first-principles calculations, we performed electrochemical impedance spectroscopy to determine the charge transfer resistance (R_{ct}) of these electrode materials.⁵¹ As shown in Fig. S8 (ESI[†]), the charge transfer resistance for the cation-disordered ZnSiP₂ (~100 Ω) is much smaller than that for the cation-ordered ZnSiP₂ (~343 Ω). On the Li-ion storage and transport properties, to optimize the structure with the lowest energy during the simulations at the level of atoms, various structural configurations of Li-ions in the lattices and interstitial sites were simulated. The involved lattices were all relaxed at each position by utilizing the primary multiple energy minimization calculation principle. Within the crystal structure of ZnSiP₂, there exist four voids, each large enough to host one Li atom. When a Li-ion hops among the voids, the activation energy was calculated using the random-cation supercell (Fig. S7a, ESI[†]). There exist eight Li-ion transportation manners endowed by different local environments brought on by the cation disordering within the simulation model. The specific Li-ion diffusion paths following octahedron–tetrahedron–octahedron sites where the site is surrounded by Si or Zn atoms and the corresponding Li-ion activation energy profiles with unsymmetrical features are both presented in Fig. S9 (ESI[†]). As listed in Fig. 2e, most of the activation energy values are below 0.6 eV. As compared in Fig. 2e and Fig. S10 (ESI[†]), however, most activation energies for the cation-ordered ZnSiP₂ are above 0.68 eV. These lower migration barriers endowed by the cation-disorder indicate more facile Li transport in the cation-disordered ZnSiP₂ anode. To validate the predictions of theoretical calculations, we used the galvanostatic intermittent titration technique (GITT) to determine Li ion diffusion coefficients in both the cation-disordered and cation-ordered ZnSiP₂ electrodes.⁵¹ As shown in Fig. S11 (ESI[†]), the average Li-ion diffusion coefficients (especially within the potential window for battery cycling) of the cation-disordered ZnSiP₂ electrode are higher than those of the cation-ordered ZnSiP₂ electrode. On the resistance to volume change produced by lithiation/delithiation, we calculated and compared the elastic constants of both cation-disordered and cation-ordered ZnSiP₂ using first-principles theory.^{50–52} As compared in Fig. 2f, the cation-disordered ZnSiP₂ is softer than the cation-ordered ZnSiP₂ since the elastic constants of the cation-disordered ZnSiP₂ are smaller than the cation-ordered ZnSiP₂ counterparts. The softer property can be mainly attributed to its cation disorder with higher symmetry. The softer property means it is easy to accommodate volume change brought on by lithiation/delithiation of the host material.^{50–52} To recap, the cation-disordered ZnSiP₂ has much faster electronic conductivity (metallic conductivity, Fig. 2d), much lower activation energy (Fig. 2e), and better mechanical stability (Fig. 2f) to structural change than the cation-ordered ZnSiP₂ counterparts. The simulation results rationalize the observed superior electrochemical performance of the cation-disordered ZnSiP₂ with respect to fast reaction kinetics,

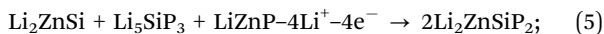
small polarization loss, and high energy efficiency compared to the cation-ordered ZnSiP₂ counterparts. This demonstrates that the cation-disordered ZnSiP₂ would be a high-performance anode material for next-generation LIBs.

To further elucidate the fundamental reasons behind the electrochemical Li-storage behaviours of the cation-disordered ZnSiP₂, the structural and compositional evolution of the electrode accompanying the lithiation/delithiation process (Fig. S12, ESI[†]) was systematically investigated *via* XRD and HRTEM along with SAED, XPS and Raman. As shown in Fig. 3a-ii, with the potential decreased to 0.43 V by discharge, all the fingerprint peaks of the cation-disordered ZnSiP₂ anode were shifted to lower 2 theta accompanied by reduced intensities. This phenomenon can be assigned to the topotactical transformation into Li_xZnSiP₂ ($x < 2$) from the pristine cation-disordered ZnSiP₂ with two voids shown in Fig. S13 (ESI[†]). From the corresponding HRTEM and SAED images shown in Fig. S14a (ESI[†]), slightly expanded crystal planes of (111) and (220) of the cation-disordered ZnSiP₂ can be observed. As the discharge proceeds, all the fingerprint peaks of the cation-disordered ZnSiP₂ disappeared thoroughly, which is due to the decomposition of Li₂ZnSiP₂ into Li₂ZnSi, Li₅SiP₃ and LiZnP as validated by the subsequent XRD data (Fig. 3a-iii). The characteristic diffraction peaks of the layered semiconducting Li₂ZnSi (crystal structure shown in Fig. S15, ESI[†]) at 26.6°, 32.6°, 44.0° and 48.2°, of Li-ion conductor Li₅SiP₃⁵⁴ at 26.3° and 51.7°, and of semiconductor LiZnP at 26.8° and 44.5° were observed, respectively. This suggests that the fresh cation-disordered ZnSiP₂ anode has been transformed into three phases of Li₂ZnSi, Li₅SiP₃, and LiZnP at the conversion stage, which was confirmed by the corresponding HRTEM and SAED analysis (Fig. S14b, ESI[†]). When discharged to a final potential of 0.005 V (Fig. 3a-iv), the above-observed ternary lithium-containing phases disappeared and spontaneously the well-indexed diffractions of Li₃P, Li_{4.4}Si and LiZn alloys appeared, presenting the formation of the final lithiation products. The formation of the final binary lithiated products can also be supported by the corresponding HRTEM images and SAED patterns as shown in Fig. S14c (ESI[†]). Based on these results, the cation-disordered ZnSiP₂ electrode can deliver *ca.* 2000 mA h g⁻¹, also coinciding with the discharge capacity. In the subsequent charge process, the XRD fingerprint signals of these binary lithium-containing Li₃P, Li_{4.4}Si and LiZn alloyed phases were dramatically weakened or disappeared with the reappearance of the fingerprint signals of the Li₂ZnSi, Li₅SiP₃, and LiZnP phases. However, when the potential was increased to 0.47 V by charging, the characteristic peaks of the re-formed Li₂ZnSi, Li₅SiP₃, and LiZnP phases were very weak due to the lost crystallinity during cycling (Fig. 3a-v and Fig. S14d, ESI[†]). All the charged observations were also well consistent with the corresponding HRTEM images and SAED patterns as shown in Fig. S14e (ESI[†]). This is presumably because these electrochemical reaction products at this stage have low crystallinity due to more Li-extraction during the charge and are well-distributed in the carbon matrix, thus rendering their X-ray signals almost invisible as shown in Fig. 3a-vi. When completely charged back to 3.0 V, the fingerprint peaks of the cation-disordered ZnSiP₂ phase have been reformed, as shown in Fig. 3a-vii and Fig. S14f (ESI[†]). In addition, the *ex situ*

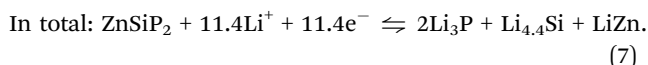
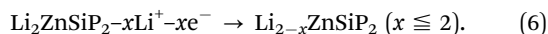
during the charge process, the initial stage (de-reconversion)



the second stage (de-conversion)



the third stage (de-intercalation)



In short, during discharge, the ZnSiP_2 electrode underwent electrochemical reactions comprised of intercalation, conversion, and re-conversion in sequence. During the charge process, all these corresponding reaction sequences appeared to be reversible, until reformation of the initial crystal structure of the cation-disordered ZnSiP_2 . Based on this peculiar Li-storage mechanism, the cation-disordered ZnSiP_2 electrode could accommodate 11.4 Li-ions per formula, corresponding to 1970 mA h g^{-1} , where the two P atoms contribute 1037 mA h g^{-1} , the one Si atom contributes 760 mA h g^{-1} , and the Zn atom donates the remaining 173 mA h g^{-1} . As estimated from the discharge/charge tests, the first discharge capacity for the cation-disordered ZnSiP_2 is *ca.* 2000 mA h g^{-1} , approaching the theoretical value, which implies the complete conversion reaction of ZnSiP_2 for Li-storage is as given in eqn (7).

To further prolong the cycle life and boost the rate performance of the cation-disordered ZnSiP_2 electrode, the material was mixed with commercial graphite *via* the facile mechanical ball milling method. The XRD diffraction peaks of the resulting ZnSiP_2/C composite (Fig. S19, ESI[†]) can be well-indexed although with a slightly reduced peak intensity and broader half-width, implying that the milling process produces enough energy to break the layered graphite to encapsulate the well-distributed ZnSiP_2 . Furthermore, the as-milled graphite composite is composed of numerous nanosized irregularly shaped particles that are well-populated within the carbon matrix (Fig. S20, ESI[†]), which agglomerate into larger microsized secondary particles with a little BET surface area of $12.4 \text{ m}^2 \text{ g}^{-1}$ (Fig. S21, ESI[†]). The featured morphology of ZnSiP_2/C inherently favors Li-storage in the following two aspects. First, the nanoparticles would facilitate electrolyte permeation along the numerous grain boundaries, where the Li-ion transfer capability is also much faster than that within the crystals, shorten the Li-ion diffusion length, and decrease the structural strain, compared with large-size single crystals and bulk samples prepared *via* solid-state calcination. Second, the large aggregated microsized particles would favor the formation of stable SEI films at the electrode/electrolyte interfaces, which could improve the initial coulombic efficiency by decreasing the side reactions brought on by nanoparticles and also help increase the tapped density to promote the energy density, compared with overlarge BET electrode materials. As seen from the HRTEM image of the ZnSiP_2/C nanocomposite, the nanosized crystalline domains of ZnSiP_2 ($< 5 \text{ nm}$) were well-embedded into the amorphous carbon matrix and distributed

evenly. As shown in Fig. 4a, the periodical lattice fringes with a *d*-spacing of 0.308 nm could be assigned to the (111) crystal plane of crystalline ZnSiP_2 particles. From the SAED pattern (the inset of Fig. 4a), we can see halo-like multiple rings with some well-dispersed spots, which indicates that a large number of ZnSiP_2 nanoparticles were well-distributed in the amorphous carbon matrix. The TEM-based energy dispersive X-ray spectroscopy (EDX, the inset of Fig. 4a) demonstrates that the atomic ratio of Zn, Si and P is approximately 1 : 1 : 2. As shown in Fig. 4b and c, the color-coded element mappings show the homogeneous distribution of Zn, Si, P and C throughout the nanocomposite, indicating that ZnSiP_2 is composited with graphite to form an ultrafine nanocomposite thanks to the presence of graphite, which alleviates the aggregation issue during the mechanical milling. The well-hybridized nanocomposite accelerates e^- and Li^+ transfer and accommodates large volume change throughout the whole electrochemical Li-storage process. As shown in Fig. 4d, ZnSiP_2/C delivered considerable cycling stability with a remaining capacity of 1789 mA h g^{-1} after 500 cycles at a current density of 200 mA g^{-1} at a potential range of 3.0–0.005 V. More impressively, as shown in Fig. S22 (ESI[†]), at a high current density of 2 A g^{-1} , the ZnSiP_2/C electrode still retained 1278 mA h g^{-1} after 2000 cycles, accounting for 84.6% of the initial reversible capacity. Also, the coulombic efficiency *vs.* cycle number plot reached 99.5% except for the initial cycle, which further indicated that the ZnSiP_2/C anode obtained inherent high reversibility for Li-storage. Moreover, ZnSiP_2/C shows excellent reversible capacity retention at different current densities (the inset of Fig. 4d). High reversible capacities of 1920 mA h g^{-1} at 0.1 A g^{-1} , 1850 mA h g^{-1} at 0.2 A g^{-1} , 1785 mA h g^{-1} at 0.3 A g^{-1} , 1730 mA h g^{-1} at 0.5 A g^{-1} , 1650 mA h g^{-1} at 1.0 A g^{-1} , 1500 mA h g^{-1} at 2.0 A g^{-1} , 1390 mA h g^{-1} at 3.0 A g^{-1} , 1250 mA h g^{-1} at 5.0 A g^{-1} , and 1010 mA h g^{-1} at 15.0 A g^{-1} could be achieved, thus showing the ultrahigh-rate capability of the ZnSiP_2/C electrode. Even at an ultrahigh current density of 30 A g^{-1} , the reversible specific capacity could reach as high as 585 mA h g^{-1} , which is still larger than the theoretical capacity of graphite (372 mA h g^{-1}). Furthermore, 98% of its first-cycle reversible capacity could be attained when the current density was decreased back to 0.1 A g^{-1} . As compared in Fig. 4e and f, the cation-disordered ZnSiP_2/C anode delivers the best performance in terms of the rate performance and first-cycle coulombic efficiencies among its related binary- or single-component anode counterparts. Moreover, as compared in Fig. 4g and h, the cycle stability and rate performance of the cation-disordered ZnSiP_2/C anode surpass all the multi-phase anodes studied.^{27,32,36,63–77} The superiority mainly benefited from the inherent merits of the cation-disordered ZnSiP_2 like the metallic conductivity, the introduced graphite carbon as a buffer matrix to accommodate the volume change during cycling and the ternary intermediate electrochemical products like Li_2ZnSi , Li_5SiP_3 and LiZnP , which also obtained inherent fast Li-ion and electron transfer capabilities.

Considering the versatility of the cation-disorder, we further expand the horizon to include a novel family of $\text{Zn}(\text{Cu})\text{-Si-P}$ based on the specific cation-disordered ZnSiP_2 case and evaluate

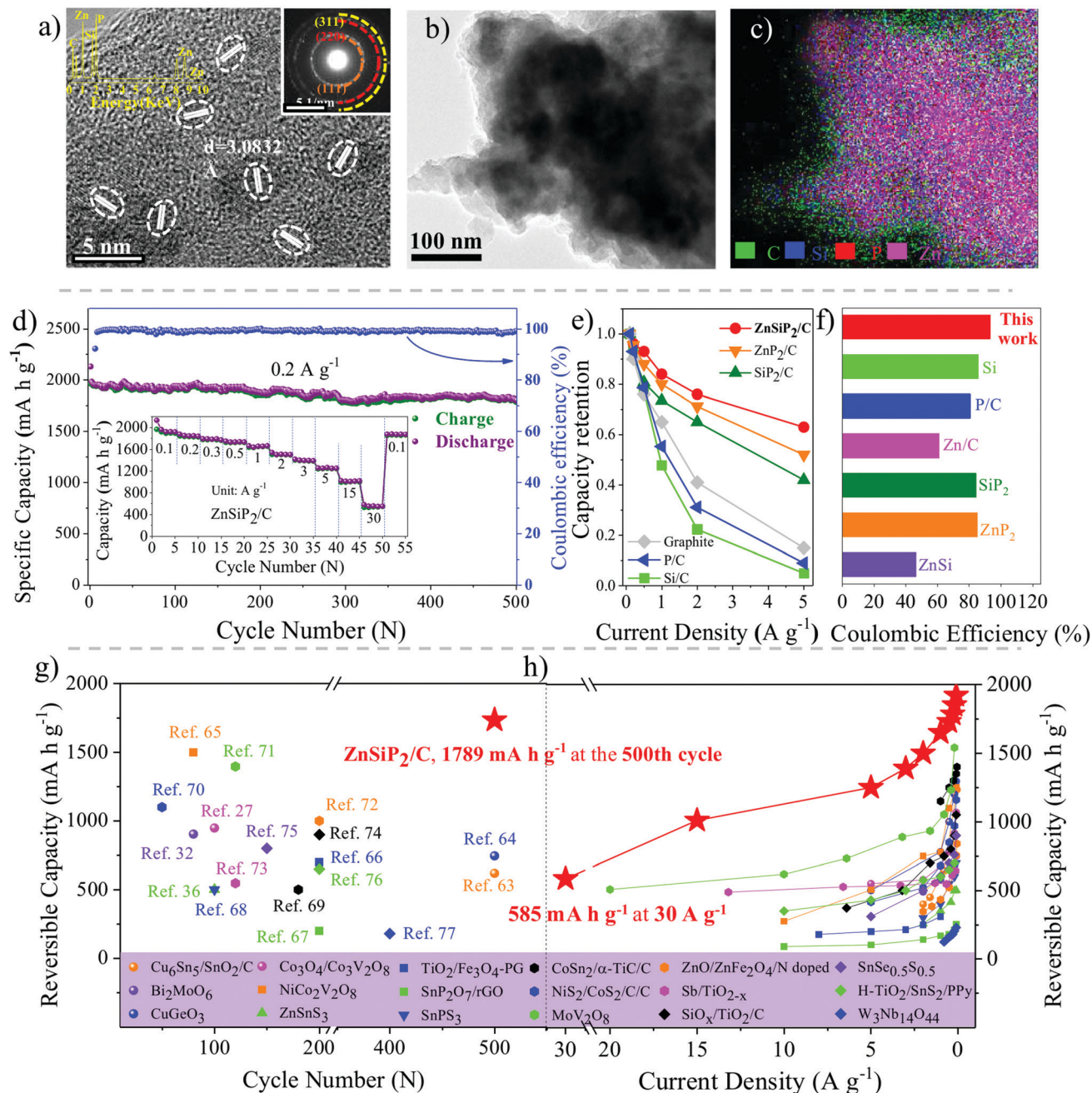


Fig. 4 (a) The high-resolution TEM image (HRTEM) of the cation-disordered $\text{ZnSiP}_2/\text{graphite}$ composite; (b) the TEM frame image used for elemental mapping of the cation-disordered $\text{ZnSiP}_2/\text{graphite}$ composite; (c) the elemental mapping of the cation-disordered $\text{ZnSiP}_2/\text{graphite}$ composite; (d) the long-cycle stability of the cation-disordered $\text{ZnSiP}_2/\text{graphite}$ composite and the inset is the rate performance; (e) the rate performance comparison of the cation-disordered $\text{ZnSiP}_2/\text{graphite}$ composite with the related binary phase graphite and single-component graphite composites prepared in our lab under the same experimental conditions; (f) the first-cycle coulombic efficiency comparison of the cation-disordered $\text{ZnSiP}_2/\text{graphite}$ composite with the related binary-component graphite and single-component graphite composites prepared in our lab under the same experimental conditions. The performance comparison of the cation-disordered ZnSiP_2/C with multi-phase anodes studied: (g) the cycle stability comparison at relatively small current densities; (h) the rate performance comparison.

their Li-storage performances. Firstly, considering the cation-disordered feature of the as-synthesized ZnSiP_2 , materials with different Zn/Si ratios were synthesized. As shown in Fig. 5a, with an increasing molar ratio of Si within the cation sites of the Zn–Si–P, all the Si-like peaks ($\text{ZnSi}_2\text{P}_3 \rightarrow \text{ZnSi}_3\text{P}_4 \rightarrow \text{ZnSi}_4\text{P}_5$) shift to higher angles (Fig. 5b), which indicates they have similar

crystal structure, but with some shrinkage due to the smaller atomic size of Si compared to Zn. Secondly, as known, Cu is located next to Zn in the Periodic Table and, moreover, as a non-competitive element with the cathode it is widely used in our daily life because of its excellent conductivity. Considering these facts and its similar atomic size, bonding characteristics and

electronegativity to those of Zn, we further replace Zn with Cu to further extend the family and meanwhile change the cation Cu/Si ratios. As expected, the Cu–Si–P ($\text{CuSi}_2\text{P}_3 \rightarrow \text{CuSi}_3\text{P}_4 \rightarrow \text{CuSi}_4\text{P}_5$) show similar structural characteristics (Fig. 5c and d) to those of the Zn–Si–P compounds. Actually, Zn(Cu)–Si–P atoms can be exchanged with each other in a large range as discussed above. All these results indicate that these cation-disordered atomic arrangements seem to involve similar atoms in a wide range. As known, the physicochemical properties including the electrochemical performance of the materials depend on the crystal structure and components and meanwhile can be greatly affected by the doping.^{57,58} Therefore, we investigate and compare the electrochemical Li-storage behaviours of the above synthesized cation-disordered family (Zn(Cu)–Si–P). As compared in Fig. 5e and f, all these cation-disordered anodes can deliver large discharge capacities within the range of 1900–2600 mA h g⁻¹

(insets of Fig. 5e), which approaches the theoretical capacity based on the corresponding binary Li-alloy products ($\text{Li}_{1.4}\text{Si}$, LiZn and Li_3P), with very high initial coulombic efficiency above 90% (insets of Fig. 5e). More importantly, all of them deliver an appropriate low and safe working potential within the range of 0.4–0.5 V vs. Li^+/Li (Fig. 5f). The working potential is above the lithium plating potential like that of silicon and graphite, which avoids the formation of dendrites impaling the separator especially at high rates. The working potential of the new anode family is not as high as that of phosphorus, which could achieve competitive energy density applied in full cells. Accordingly, we develop a novel family of cation-disordered anode materials with a more practical working potential filling the gap between that of silicon and P/C composites, thus meeting the demands of both high safety and high energy density when applied in full cells.

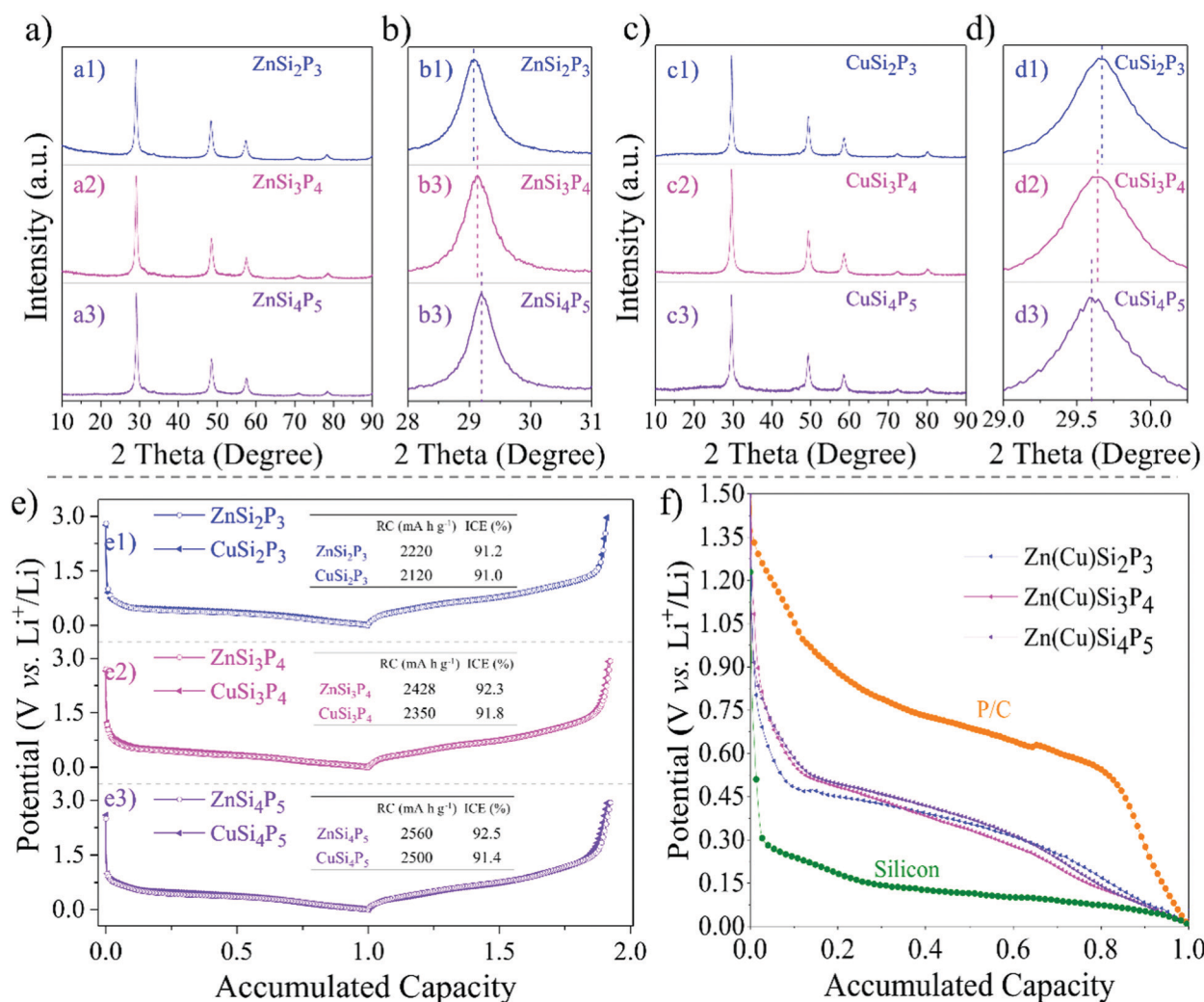


Fig. 5 (a) The XRD patterns of the ternary cation-disordered Zn–Si–P compounds ($\text{ZnSi}_2\text{P}_3 \rightarrow \text{ZnSi}_3\text{P}_4 \rightarrow \text{ZnSi}_4\text{P}_5$); (b) the enlarged XRD patterns of the first strongest peak to identify the shift of peak position. (c) The XRD patterns of the ternary cation-disordered Cu–Si–P compounds ($\text{CuSi}_2\text{P}_3 \rightarrow \text{CuSi}_3\text{P}_4 \rightarrow \text{CuSi}_4\text{P}_5$); (d) the enlarged XRD patterns of the first strongest peak to identify the shift of peak position. (e) The initial discharge/charge profile comparison of the ternary cation-disordered Zn–Si–P with Cu–Si–P compounds; (f) the typical discharge profile comparison of the above Zn(Cu)–Si–P family with P/C and Si anodes. Note that “RC” means reversible capacity and “ICE” means initial coulombic efficiency.

In summary, we synthesized new cation-disordered ZnSiP₂ by a facile ball milling method. When used as an anode for LIBs, the cation-disordered ZnSiP₂ anode delivers enhanced Li-storage properties compared to those of the cation-ordered ZnSiP₂ in term of reaction kinetics and energy efficiency. The superiority is attributed to the faster transport of e⁻ and Li⁺ and the better endurance to volume variation of the cation-disordered ZnSiP₂ than the cation-ordered ZnSiP₂ counterparts, as confirmed by first-principles calculations and electrochemical impedance spectroscopy. The cation-disordered cubic ZnSiP₂ undergoes intercalation, conversion, and re-conversion reactions. During the de-lithiation process, all the lithiation reactions are reversed, including the structural evolution, until the original crystal structure is re-constructed, as confirmed by XRD along with HRTEM, Raman, XPS, and electrochemical measurements. The carbon composite (ZnSiP₂/C) achieves long-term cyclability (a reversible capacity of 1278 mA h g⁻¹ after 2000 cycles at a current density of 2000 mA g⁻¹, accounting for 84.6% of the initial reversible capacity) and high-rate performance (585 mA h g⁻¹ at 30 A g⁻¹). The cycle and rate performance surpass all the reported multi-phase anodes studied. These superior performances also benefit from the synergetic Li-storage capability of each component and the intermediate electrochemical products like Li₂ZnSi, Li₅SiP₃ and LiZnP, which have excellent electron and Li-ion transfer capability. Furthermore, the introduced graphite provides not only a continuous network for efficient current collection but also a structural framework for accommodation of the volume changes during Li-ion insertion/retraction. The concept of the cation-disordered ZnSiP₂ can be further extended to a family of cation-disordered Zn(Cu)-Si-P materials with a wide range of cation ratios, which have never before been synthesized. All these materials show large capacity, high initial coulombic efficiency, and proper working potentials between those for P/C and Si anodes.

Experimental section

Material preparation

All these cation-disordered Zn(Cu)-Si-P (including ZnSiP₂, ZnSi₂P₃, ZnSi₃P₄, ZnSi₄P₅, CuSi₂P₃, CuSi₃P₄, and CuSi₄P₅) samples were prepared by a low-cost and scalable mechanical ball milling method with sealed element powders in a given ratio in a vessel with a protection gas of argon. To obtain a high impact energy, the selected grinding bowl with a volume of 500 mL and grinding balls with a diameter of 10 mm are both stainless steel. The grinding balls and a mixture of Zn(Cu), Si and red P (3 g) were placed in the grinding bowl in sequence. The material to steel ball mass ratio is 1:25. When ground by a planetary mono mill (Fritsch Pulverisette-6) at a speed of 300 rpm, the milling duration is 10 min with resting for 5 min. To obtain better mechanical alloying, the reversing operation mode (regular reversal of the direction of rotation) is adopted. The cation-ordered ZnSiP₂ was synthesized by CVT as reported before.^{42,43} When serving as anodes, it was ball milled under the same experimental conditions as those of the cation-disordered ZnSiP₂. The ZnSiP₂/C, the related single-component carbon composites (P/C, Si/C, and Zn/C),

and the related binary-component carbon composites (ZnP₂/C, ZnSi/C, and SiP₂/C) were also synthesized by further milling the as-prepared compounds with commercial graphite in a mass ratio of 7:2 for a duration of 2.0 h under similar experimental conditions.

Material characterization

All these samples were studied by X-ray diffraction (PANalytical X'pert PRO-DY2198 with Cu-K α radiation). The related morphology was observed using a field-emission scanning electron microscope (FSEM, FEI Quanta650), and the micro-structures were detected using a transmission electron microscope (TEM, JEOL JEM 2100) including a high resolution transmission electron microscope (HRTEM) and selected area electron diffraction (SAED). The related valence and composition analysis were carried out *via* X-ray photoelectron spectroscopy (Thermo Fisher ESCA-Lab250 with monochromatic 150 W AlK α radiation). The related Raman data were collected using a confocal Raman spectrometer (Raman, WTEC ALPHA300 with a 532 nm excitation laser).

Electrochemical characterization

For the pure phase, all these active materials were milled with carbon black and Li-PAA in a mass ratio of 7:2:1. The slurries were pasted onto copper foil and dried under a vacuum at 100 °C for 24 h. For the related carbon composites, these composites were directly milled with Li-PAA in a 9:1 mass ratio. The loading materials were 1.8–2 mg cm⁻². The diameter of the electrode is 8 mm. The electrochemical characterization was conducted utilizing coin-type cells (CR2032) sealed in a glovebox (Mbraun, Labmaster 130) full of argon, where the contents of O₂ and H₂O were both controlled under 0.01 ppm. Li foil served as the counter and reference electrodes, and the related electrolyte was 1 M LiPF₆ dissolved in EC/DEC (1:1 by volume). The Li-storage discharge/charge tests were conducted on a LAND battery tester (Wuhan Kingnuo Electronic Co., China) and on a testing system (Hokuto Denko, HJ1001SD8). The cyclic voltammetry (CV) measurements were conducted on an electrochemical workstation (Autolab, Pgstat 302N). As for the accumulated capacity, the test conditions are as usual: the cycling rate was 200 mA g⁻¹ in a potential range of 3.0–0.005 V. In order to compare the electrochemical behaviors, both the discharge and charge capacity were normalized to the initial discharge capacity.

Calculation details

First-principles calculations was carried out using VASP (Vienna Ab-initio Simulation Package).⁵⁹ The exchange–correlation functional with the generalized gradient approximation parameterized by Perdew, Burke and Ernzerhof was used.⁶⁰ The core-electrons were kept frozen in the form of a projector augmented wavefunction,⁶¹ with the valence electron configuration for P 3s²3p³, Si 3s²3p², and Zn 3d¹⁰4s². A 4 × 4 × 4 Monkhorst–Pack reciprocal grid, together with a 400 eV energy cutoff, was used for sufficient energy calculations.⁶² Gaussian smearing with a smearing width of 0.05 eV was used to accelerate the computation of the electronic energy near the Fermi level.

Conflicts of interest

There are no conflicts to declare.

Acknowledgements

This work was supported by the National Natural Science Foundation of China (21701030, 51801096), Guangdong Province Natural Science Foundation (2017A030310241), innovative talents cultivation project of outstanding youth in Guangdong Province (2016KQNCX038), Science and Technology Planning Project of Guangzhou City (201804010392), China Postdoctoral Science Foundation funded project (No. 1112000139), Guangdong Innovative and Entrepreneurial Research Team Program (No. 2014ZT05N200), and US National Science Foundation (DMR-1742828). The authors acknowledge the use of facilities at Guangdong University of Technology, Georgia Institute of Technology, and Southern University of Science and Technology. The computational work used resources of the National Energy Research Scientific Computing Center (NERSC), a U.S. Department of Energy Office of Science User Facility operated under Contract No. DE-AC02-05CH11231.

References

- 1 Y. Wei, L. Huang, J. He, Y. Guo, R. Qin, H. Li and T. Zhai, *Adv. Energy Mater.*, 2018, **8**, 1703635.
- 2 Q. Xu, J. Li, J. Sun, Y. Yin, L. Wan and Y. Guo, *Adv. Energy Mater.*, 2017, **7**, 1601481.
- 3 W. Li, Y. Yang, G. Zhang and Y. Zhang, *Nano Lett.*, 2015, **15**, 1691–1697.
- 4 W. Chang, K. Tseng and H. Tuan, *Nano Lett.*, 2017, **17**, 1240–1247.
- 5 J. Zhou, X. Liu, W. Cai, Y. Zhu, J. Liang, K. Zhang, Y. Lan, Z. Jiang, G. Wang and Y. Qian, *Adv. Mater.*, 2017, **29**, 1700214.
- 6 Q. Xiao, Q. Zhang, Y. Fan, X. Wang and R. A. Susantyo, *Energy Environ. Sci.*, 2014, **7**, 2261–2268.
- 7 J. Lee, Y. Ko, M. Shin, H. Song, N. Choi, M. Kim and S. Park, *Energy Environ. Sci.*, 2015, **8**, 2075–2084.
- 8 X. Li, P. Yan, X. Xiao, J. Woo, C. Wang, J. Liu and J. Zhang, *Energy Environ. Sci.*, 2017, **10**, 1427–1434.
- 9 J. H. Lee, C. S. Yoon, J. Y. Hwang, S. J. Kim., F. Maglia, P. Lamp, S. T. Myung and Y. K. Sun, *Energy Environ. Sci.*, 2016, **9**, 2152–2158.
- 10 S. Chae, M. Ko, S. Park, N. Kim, J. Ma and J. Cho, *Energy Environ. Sci.*, 2016, **9**, 1251–1257.
- 11 N. Lin, Y. Han, J. Zhou, K. Zhang, T. Xu, Y. Zhu and Y. Qian, *Energy Environ. Sci.*, 2015, **8**, 3187–3191.
- 12 Y. Jin, S. Li, A. Kushima, X. Zheng, Y. Sun, J. Xie, J. Sun, W. Xue, G. Zhou, J. Wu, F. Shi, R. Zhang, Z. Zhu, K. So, Y. Cui and J. Li, *Energy Environ. Sci.*, 2017, **10**, 580–592.
- 13 D. Lin, Z. Lu, P. Hsu, H. R. Lee, N. Liu, J. Zhao, H. Wang, C. Liu and Y. Cui, *Energy Environ. Sci.*, 2015, **8**, 2371–2376.
- 14 Q. Zhang, H. Chen, L. Luo, B. Zhao, H. Luo, X. Han, J. Wang, C. Wang, Y. Yang, T. Zhu and M. Liu, *Energy Environ. Sci.*, 2017, **10**, 580–592.
- 15 C. Du, C. Gao, G. Yin, M. Chen and L. Wang, *Energy Environ. Sci.*, 2011, **4**, 1037–1042.
- 16 S. Liu, J. Feng, X. Bian, J. Liu, H. Xu and Y. An, *Energy Environ. Sci.*, 2017, **10**, 1222–1233.
- 17 W. Zhang, J. Mao, S. Li, Z. Chen and Z. Guo, *J. Am. Chem. Soc.*, 2017, **139**, 3316–3319.
- 18 L. Chen, G. Zhou, Z. Liu, X. Ma, J. Chen, Z. Zhang, X. Ma, F. Li, H. Cheng and W. Ren, *Adv. Mater.*, 2016, **28**, 510–517.
- 19 Z. Huang, H. Hou, Y. Zhang, C. Wang, X. Qiu and X. Ji, *Adv. Mater.*, 2017, **29**, 1702372.
- 20 W. Li, S. Hu, X. Luo, Z. Li, X. Sun, M. Li, F. Liu and Y. Yu, *Adv. Mater.*, 2017, **29**, 1605820.
- 21 J. Liu, P. Kopold, C. Wu, P. A. Van Aken, J. Maier and Y. Yu, *Energy Environ. Sci.*, 2015, **8**, 3531–3538.
- 22 S. Liu, J. Feng, X. Bian, J. Liu, H. Xu and Y. An, *Energy Environ. Sci.*, 2017, **10**, 1222–1233.
- 23 Y. Liu, A. Zhang, C. Shen, Q. Liu, X. Cao, Y. Ma, L. Chen, C. Lau, T. Chen, F. Wei and C. Zhou, *ACS Nano*, 2017, **11**, 5530–5537.
- 24 J. Ni, L. Li and J. Lu, *ACS Energy Lett.*, 2018, **3**, 1137–1144.
- 25 R. Hu, Y. Ouyang, T. Liang, H. Wang, J. Liu, J. Chen, C. Yang, L. Yang and M. Zhu, *Adv. Mater.*, 2017, **29**, 1605006.
- 26 W. Zhang, J. Mao, W. Pang, Z. Guo and Z. Chen, *Electrochim. Acta*, 2017, **235**, 107–113.
- 27 Y. Lu, L. Yu, M. Wu, Y. Wang and X. Lou, *Adv. Mater.*, 2018, **30**, 1702875.
- 28 D. Pham-Cong, J. Choi, J. Yun, A. Bandarenka, J. Kim, P. Braun, S. Jeong and C. Cho, *ACS Nano*, 2017, **11**, 1026–1033.
- 29 C. Chen, X. Xie, B. Anasori, A. Sarycheva, T. Makaryan, M. Zhao, P. Urbankowski, L. Miao, J. Jiang and Y. Gogotsi, *Angew. Chem.*, 2018, **57**, 1846–1850.
- 30 S. Cao, Z. Xue, C. Yang, J. Qin, L. Zhang, P. Yu, S. Wang, Y. Zhao, X. Zhang and R. Liu, *Nano Energy*, 2018, **50**, 25–34.
- 31 P. Wu, A. Zhang, L. Peng, F. Zhao, Y. Tang, Y. Zhou and G. Yu, *ACS Nano*, 2018, **12**, 759–767.
- 32 Y. Zheng, T. Zhou, X. Zhao, W. Pang, H. Gao, S. Li, Z. Zhou, H. Liu and Z. Guo, *Adv. Mater.*, 2017, **29**, 1700396.
- 33 K. J. Griffith, K. M. Wiaderek, G. Cibir, L. E. Marbella and C. P. Grey, *Nature*, 2018, **559**, 556–563.
- 34 X. Wang, D. Chen, Z. Yang, X. Zhang, C. Wang, J. Chen, X. Zhang and M. Xue, *Adv. Mater.*, 2016, **28**, 8645–8650.
- 35 Z. Li, M. Asif, X. Huang, T. Tang and Y. Hou, *Adv. Mater.*, 2018, **30**, 1802745; A. AbdelHamid, J. Soh, Y. Yu and J. Ying, *Nano Energy*, 2018, **44**, 399–410.
- 36 X. Liu, Y. Hao, J. Shu, H. Sari, L. Lin, H. Kou, J. Li, W. Liu, B. Yan, D. Li, J. Zhang and X. Li, *Nano Energy*, 2019, **57**, 414–423.
- 37 A. D. Martinez, A. N. Fioretti, E. S. Toberer and A. C. Tamboli, *J. Mater. Chem. A*, 2017, **5**, 11418–11435.
- 38 A. D. Martinez, E. L. Warren, P. Gorai, K. A. Borup, D. Kuciauskas, P. C. Dippo, B. R. Ortiz, R. T. Macaluso, S. D. Nguyen, A. L. Greenaway, S. W. Boettcher, A. G. Norman, V. Stevanović, E. S. Toberer and A. C. Tamboli, *Energy Environ. Sci.*, 2016, **9**, 1031–1041.
- 39 A. D. Martinez, E. M. Miller, A. G. Norman, R. R. Schnep, N. Leick, C. Perkins, P. Stradins, E. S. Toberer and A. C. Tamboli, *J. Mater. Chem. C*, 2018, **6**, 2696–2703.

- 40 V. S. Bhadram, L. Krishna, E. S. Toberer, R. Hrubciak, E. Greenberg, V. B. Prakapenka and T. A. Strobel, *Appl. Phys. Lett.*, 2017, **110**, 182106.
- 41 S. Nakatsuka and Y. Nose, *J. Phys. Chem. C*, 2017, **121**, 1040–1046.
- 42 D. O. Scanlon and A. Walsh, *Appl. Phys. Lett.*, 2012, **100**, 251911.
- 43 M. A. Ryan, M. W. Peterson, D. L. Williamson, J. S. Frey, G. E. Maciel and B. A. Parkinson, *J. Mater. Res.*, 1987, **2**, 528–537.
- 44 H. H. Heenen, C. Scheurer and K. Reuter, *Nano Lett.*, 2017, **17**, 3884–3888.
- 45 J. Sun, H. Lee, M. Pasta, H. Yuan, G. Zheng, Y. Sun, Y. Li and Y. Cui, *Nat. Nanotechnol.*, 2015, **10**, 980–985.
- 46 K. Zhang, M. Park, L. Zhou, G. Lee, W. Li, Y. Kang and J. Chen, *Adv. Funct. Mater.*, 2016, **26**, 6728–6735.
- 47 K. Zhang, M. Park, L. Zhou, G. Lee, J. Shin, Z. Hu, S. Chou, J. Chen and Y. Kang, *Angew. Chem.*, 2016, **55**, 12822–12826.
- 48 M. S. Islam and G. A. J. Fisher, *Chem. Soc. Rev.*, 2014, **43**, 185–204.
- 49 Q. Bai, L. Yang, H. Chen and Y. Mo, *Adv. Energy Mater.*, 2018, **8**, 1702998.
- 50 K. Duho, K. Zhang, J. Lim, G. Lee, K. Cho, M. Cho and Y. Kang, *Mater. Today Energy*, 2018, **9**, 126–136.
- 51 D. Kim, K. Zhang, M. Cho and Y.-M. Kang, *Energy Environ. Sci.*, 2019, **12**, 1326–1333.
- 52 K. Zhang, D. Kim, Z. Hu, M. Park, G. Noh, Y. Yang, J. Zhang, V. W.-H. Lau, S.-L. Chou, M. Cho, S.-Y. Choi and Y.-M. Kang, *Nat. Commun.*, 2019, **10**, 5203.
- 53 A. Zunger, S. Wei, L. Ferreira and J. E. Bernard, *Phys. Rev. Lett.*, 1990, **65**, 353–356.
- 54 M. S. A. Haffner, T. Bräuniger and D. Johrendt, *Angew. Chem.*, 2016, **55**, 13585–13588.
- 55 J. Liu, W. Pang, T. Zhou, L. Chen, Y. Wang, V. K. Peterson, Z. Yang, Z. Guo and Y. Xia, *Energy Environ. Sci.*, 2017, **10**, 1456–1464.
- 56 Z. Ali, M. Asif, X. Huang, T. Tang and Y. Hou, *Adv. Mater.*, 2018, **30**, 1802745.
- 57 C. Yan, G. Chen, X. Zhou, J. Sun and C. Lv, *Adv. Funct. Mater.*, 2016, **26**, 1428–1436.
- 58 B. Hou, Y. Wang, D. Liu, Z. Gu, X. Feng, H. Fan, T. Zhang, C. Lü and X. Wu, *Adv. Funct. Mater.*, 2018, **28**, 1805444.
- 59 G. Kresse and J. Furthmüller, *Phys. Rev. B: Condens. Matter Mater. Phys.*, 1996, **54**, 11169–11186.
- 60 J. P. Perdew, K. Burke and M. Ernzerhof, *Phys. Rev. Lett.*, 1996, **77**, 3865–3868.
- 61 G. Kresse, *Phys. Rev. B: Condens. Matter Mater. Phys.*, 1999, **59**, 1758–1775.
- 62 J. D. Pack and H. J. Monkhorst, *Phys. Rev. B: Solid State*, 1977, **16**, 1748–1749.
- 63 R. Hu, G. H. Waller, Y. Wang, Y. Chen, C. Yang, W. Zhou, M. Zhu and M. Liu, *Nano Energy*, 2015, **18**, 232–244.
- 64 Y. Liu, T. Zhou, Y. Zheng, Z. He, C. Xiao, W. K. Pang, W. Tong, Y. Zou, B. Pan, Z. Guo and Y. Xie, *ACS Nano*, 2017, **11**, 8519–8526.
- 65 Y. Lu, J. Nai and X. W. D. Lou, *Angew. Chem.*, 2018, **57**, 2899–2903.
- 66 L. Pan, X.-D. Zhu, X.-M. Xie and Y.-T. Liu, *Adv. Funct. Mater.*, 2015, **25**, 3341–3350.
- 67 J. Pan, S. Chen, D. Zhang, X. Xu, Y. Sun, F. Tian, P. Gao and J. Yang, *Adv. Funct. Mater.*, 2018, **28**, 1804672.
- 68 E. Edison, A. Chaturvedi, H. Ren, S. Sreejith, C. T. Lim and S. Madhavi, *ACS Appl. Energy Mater.*, 2018, **1**, 5772–5778.
- 69 M.-G. Park, D.-H. Lee, H. Jung, J.-H. Choi and C.-M. Park, *ACS Nano*, 2018, **12**, 2955–2967.
- 70 Y. Lin, Z. Qiu, D. Li, S. Ullah, H. Yang, H. Xin, W. Liao, B. Yang, H. Fan, J. Xu and C. Zhu, *Energy Storage Mater.*, 2018, **11**, 67–74.
- 71 H. Zheng, Q. Zhang, H. Gao, W. Sun, H. Zhao, C. Feng, J. Mao and Z. Guo, *Energy Storage Mater.*, 2019, DOI: 10.1016/j.ensm.2019.01.005.
- 72 Y. Ma, Y. Ma, D. Geiger, U. Kaiser, H. Zhang, G.-T. Kim, T. Diemant, R. J. Behm, A. Varzi and S. Passerini, *Nano Energy*, 2017, **42**, 341–352.
- 73 N. Wang, Z. Bai, Y. Qian and J. Yang, *Adv. Mater.*, 2016, **28**, 4126–4133.
- 74 Z. Li, H. Zhao, P. Lv, Z. Zhang, Y. Zhang, Z. Du, Y. Teng, L. Zhao and Z. Zhu, *Adv. Funct. Mater.*, 2018, **28**, 1605711.
- 75 Q. Tang, Y. Cui, J. Wu, D. Qu, A. P. Baker, Y. Ma, X. Song and Y. Liu, *Nano Energy*, 2017, **41**, 377–386.
- 76 L. Wu, J. Zheng, L. Wang, X. Xiong, Y. Shao, G. Wang, J.-H. Wang, S. Zhong and M. Wu, *Angew. Chem.*, 2019, **58**, 811–815.
- 77 L. Yan, J. Shu, C. Li, X. Cheng, H. Zhu, H. Yu, C. Zhang, Y. Zheng, Y. Xie and Z. Guo, *Energy Storage Materials*, 2019, **16**, 535–544.